Figures

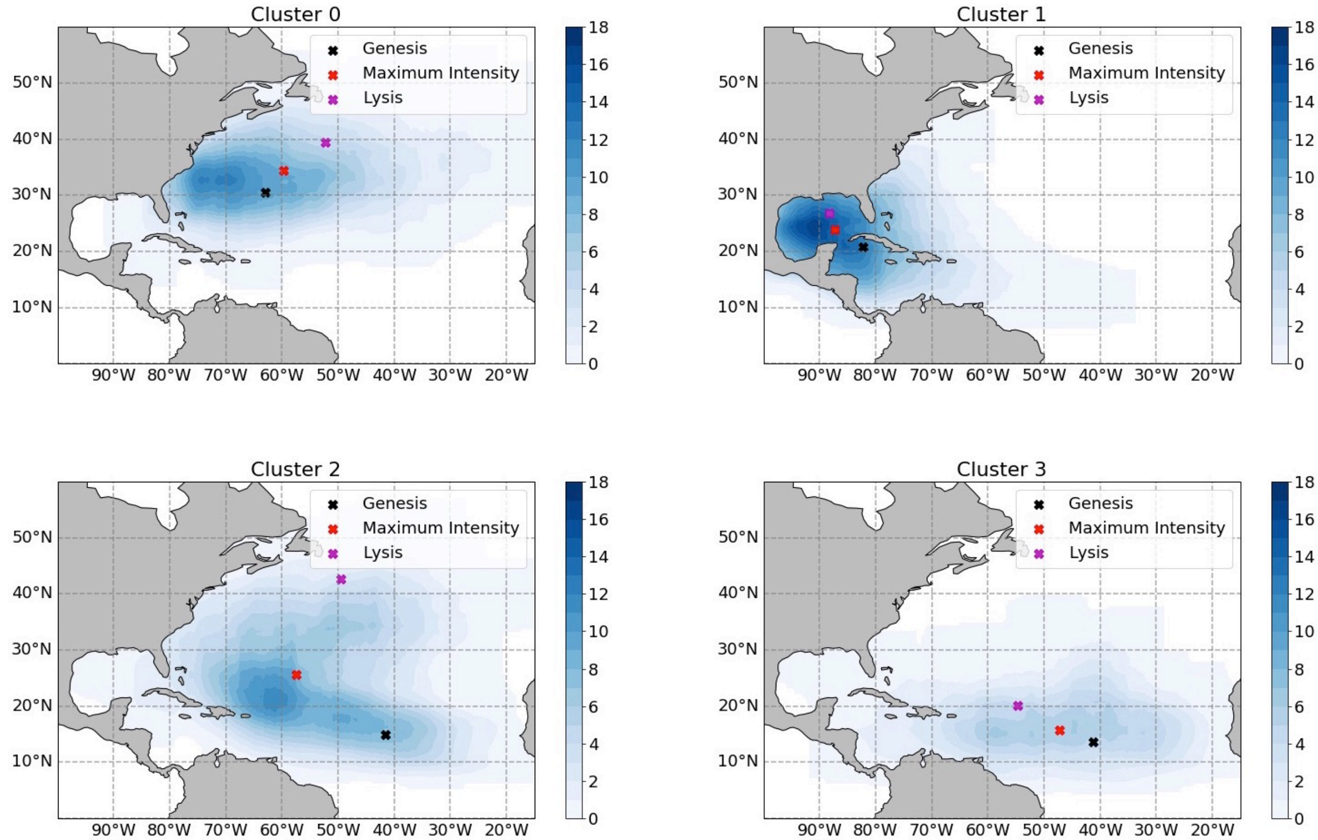

Fig. 1 TC density for each cluster, defined by the number of TC 6-hourly positions per year over a 10°x10° box centered at each location. Also shown are the average locations of genesis, maximum intensity and lysis for each cluster

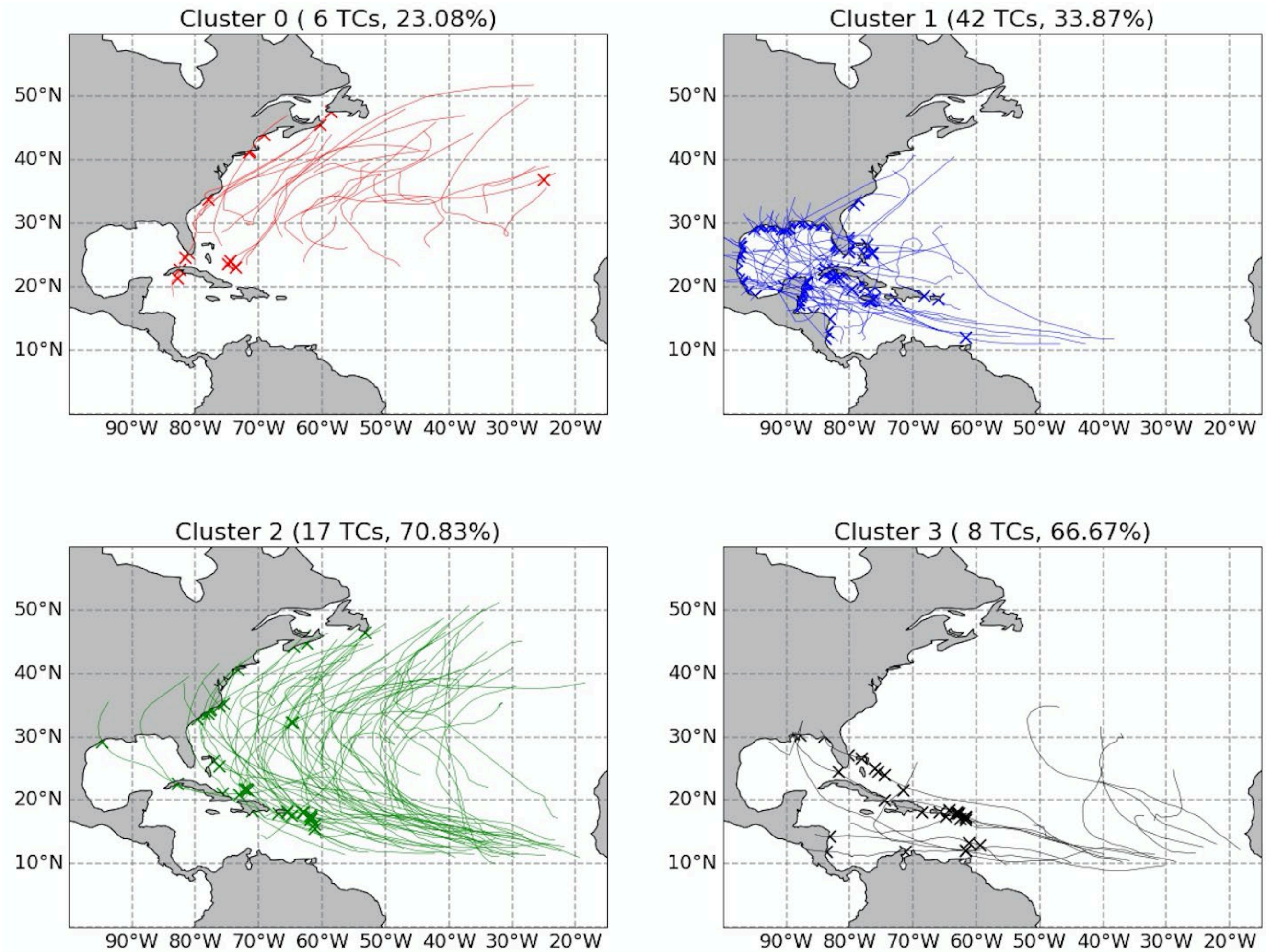

Fig. 2 Tracks of TCs that experience RI, in each cluster in the North Atlantic. Crosses indicate landfall positions of these TCs, as indicated in the HURDAT2 dataset. The title in each subplot indicates the number of such landfalling RI TCs, and the percentage of landfall TCs that experience RI

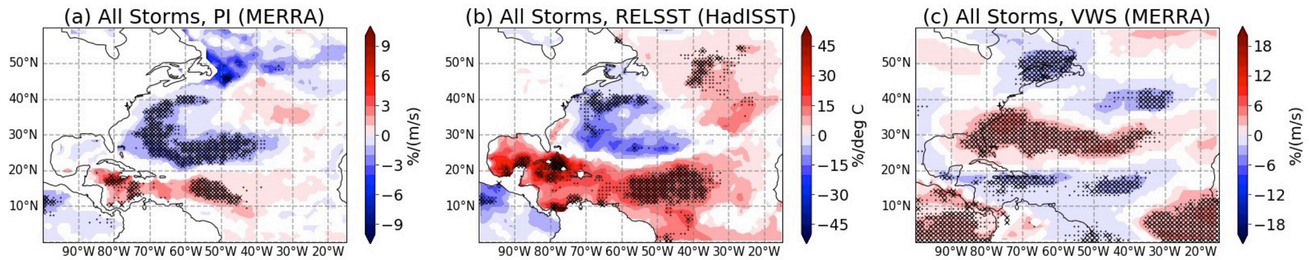

Fig. 3 Slope of the linear (median of pairwise slopes) regression of JJASON-mean MERRA PI, HadISST RELSST and MERRA VWS with RI probability, for all TCs in the North Atlantic. Regressions at 95% statistical significance are shaded in crosses, while those at 90% are shaded in dots

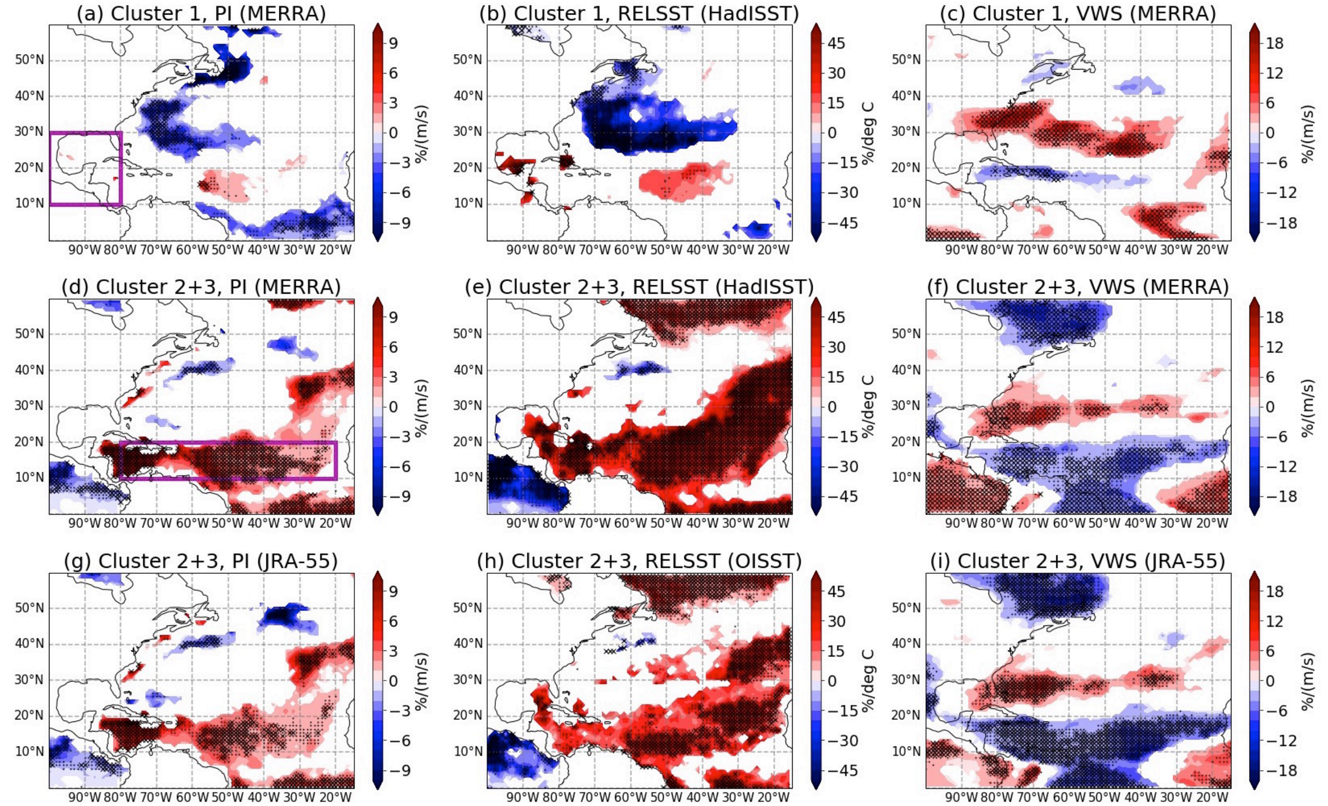

Fig. 4 Slope of the linear (median of pairwise slopes) regression of JJASON-mean MERRA PI, HadISST RELSST and MERRA VWS with RI probability, for (a-c) C1 and (d-f) C23. The magenta boxes indicate areas over which averages for C1 and C23 are computed. (g-i) As in (d-f), but for PI, RELSST and VWS from JRA-55 and NOAA OISST. Regressions at 95% statistical significance are shaded in crosses, while those at 90% are shaded in dots

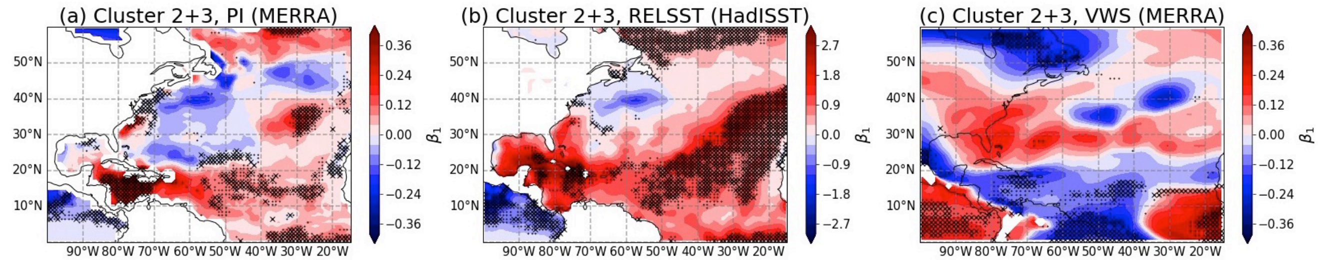

Fig. 5 As in Figure 4d-f, but for logistic regression with the slope parameter β_1 plotted

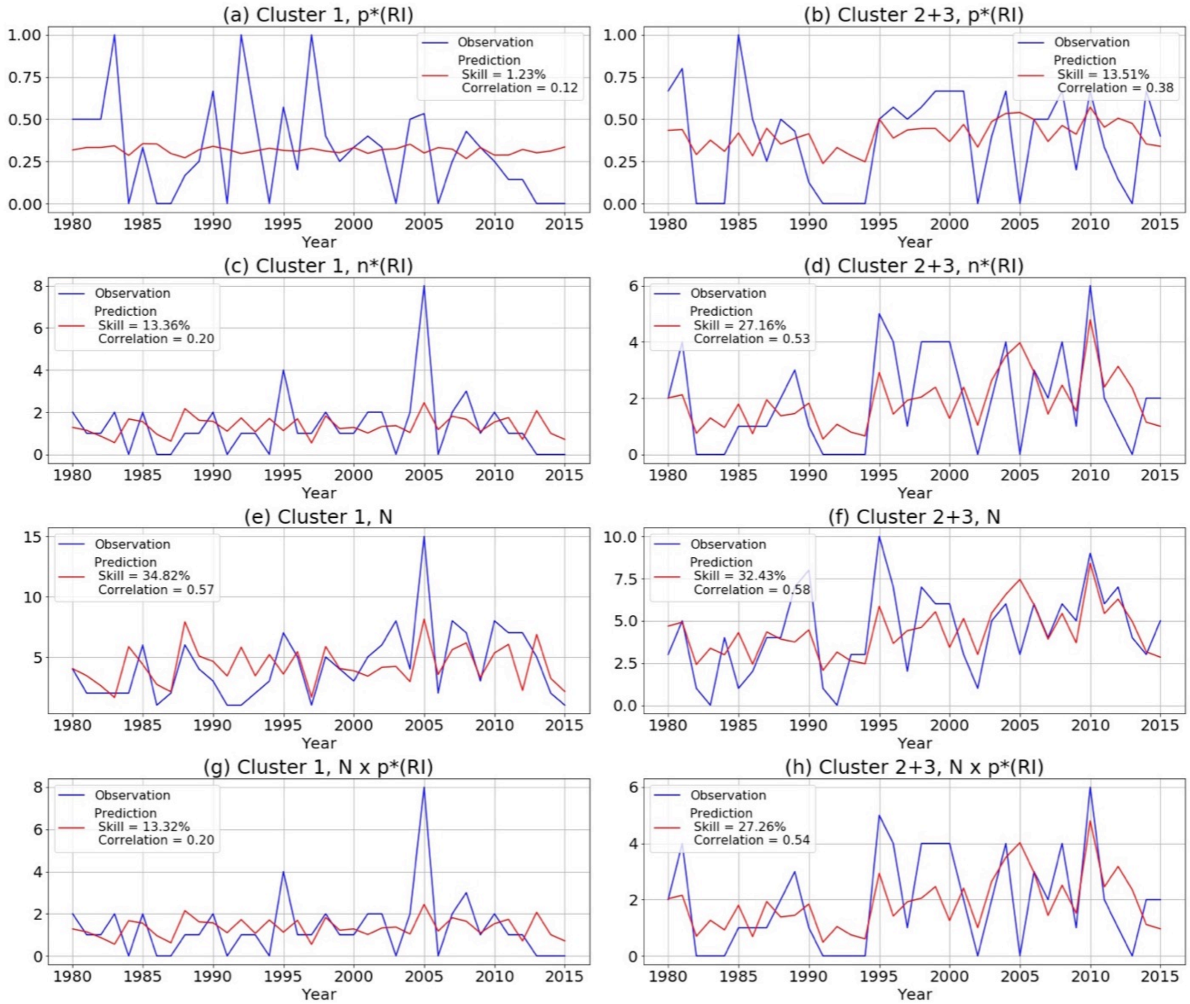

Fig. 6 Observed and predicted (a-b) RI probability ($p^{*}(RI)$, predicted with the binary logistic regression), (c-d) RI counts ($n^{*}(RI)$, predicted with the Poisson regression) and (e-f) TC counts (N, predicted with the Poisson regression), for C1 and C23. (g-h) Prediction for RI counts in C1 and C23 calculated as the product of predicted RI probability and predicted TC counts

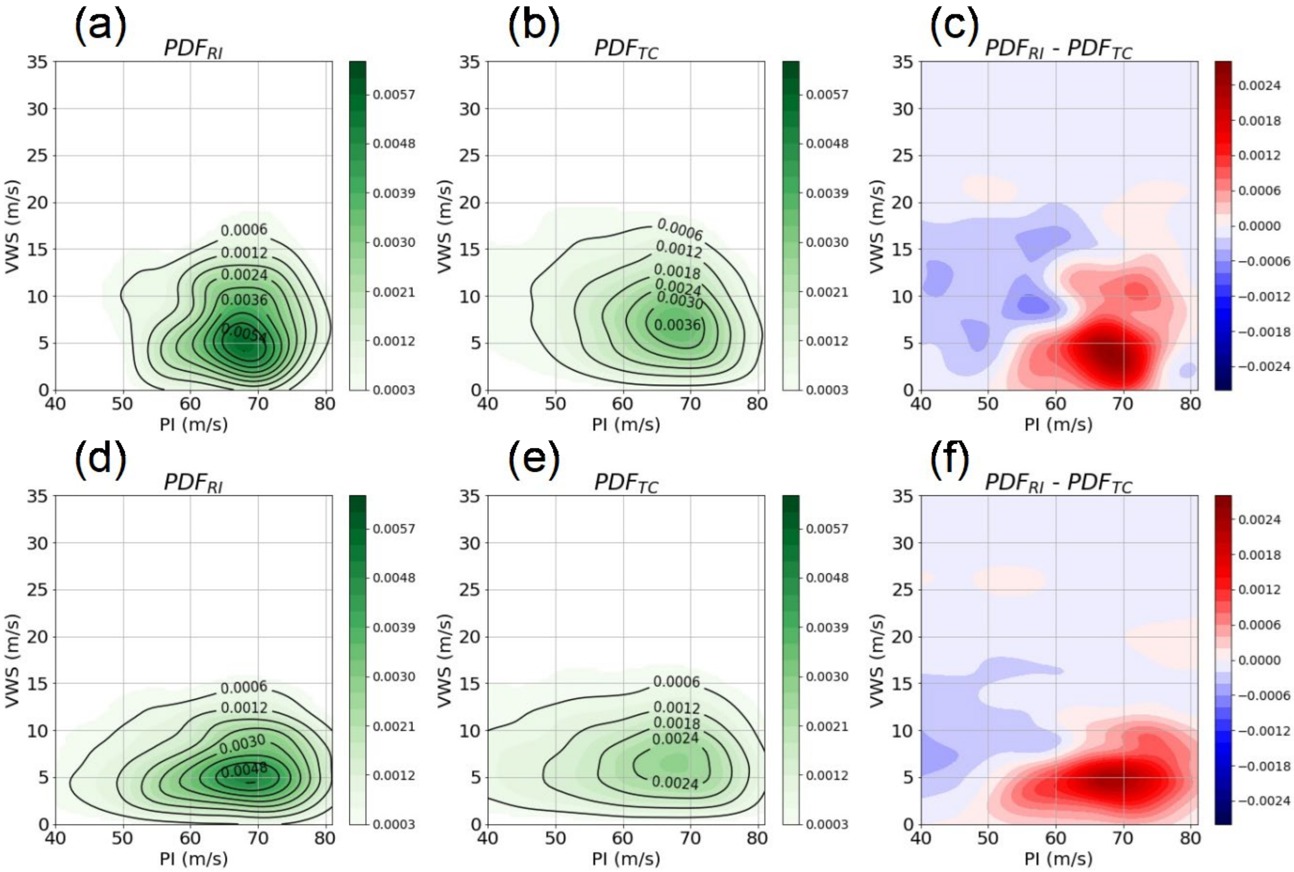

Fig. 7 The typical large-scale environment in which RI and TCs exist. The green shading and contours show the two-dimensional probability density function (a) PDF_{RI}, for all 134 RI occurrences in C1 and C23 during the period of 1980-2015, and (b) PDF_{TC}, for all TCs in C1 and C23 during the same period. (c) The difference between PDF_{RI} and PDF_{TC}. (d-f) As in (a-c), but for all 768 RI occurrences and all TCs in the North Atlantic, Northeast Pacific and Northwest Pacific combined

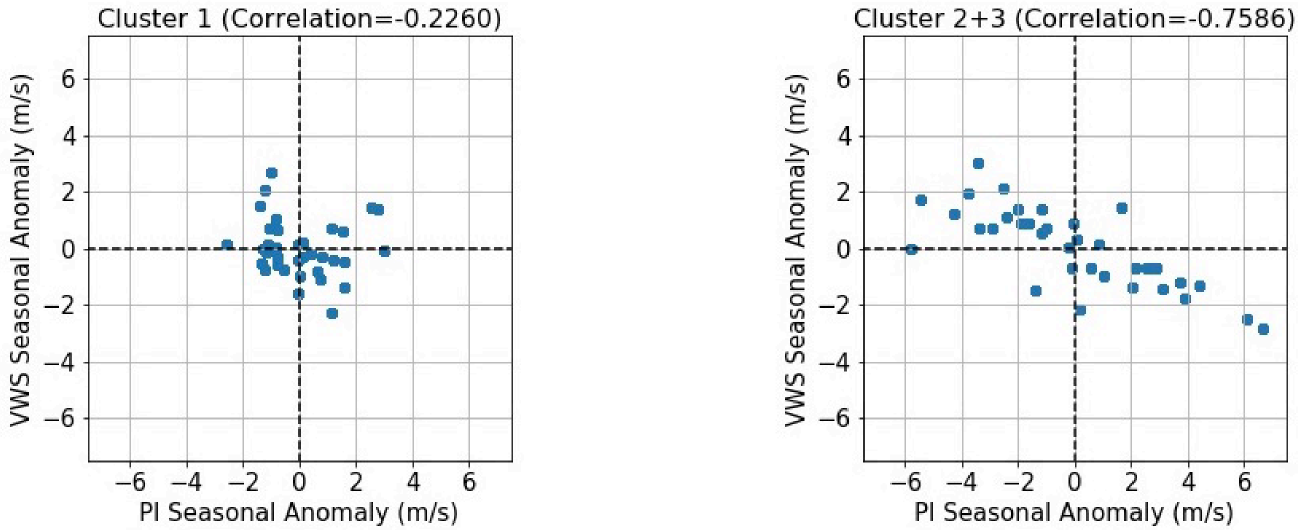

Fig. 8 Interannual variability $\langle X \rangle$ of VWS and PI values in C1 (left) and C23 (right), where each dot represents one JJASON season. Seasonal anomalies of VWS and PI are more negatively correlated in C23 than C1

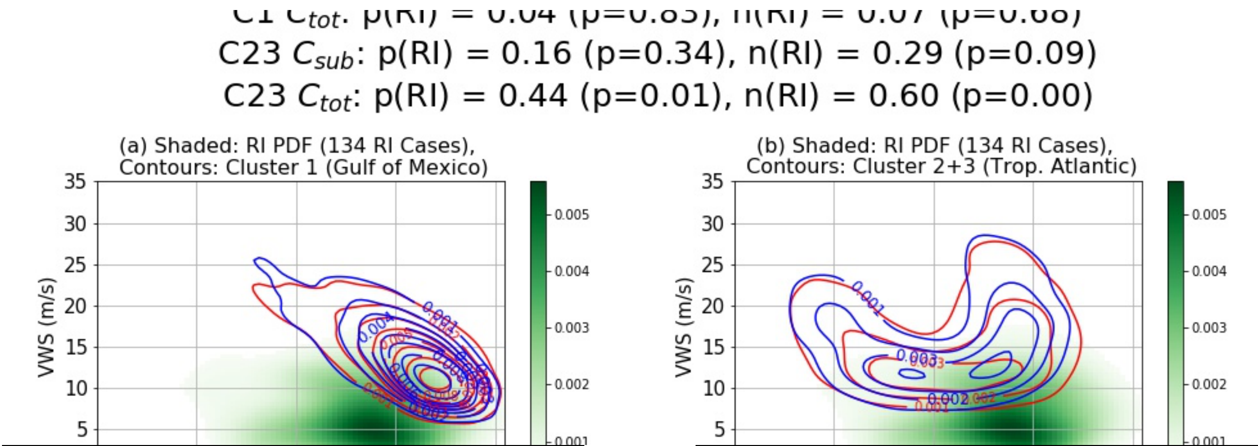

	$p(RI)$		$n(RI)$	
	corr	p	corr	p
C_{sub}	0.07	0.70	-0.10	0.56
C_{tot}	0.04	0.83	0.07	0.68

	$p(RI)$		$n(RI)$	
	corr	p	corr	p
C_{sub}	0.16	0.34	0.29	0.09
C_{tot}	0.44	0.01	0.60	0.00

Fig. 9 Reconstruction of RI seasonal statistics without and with interannual variability of the large-scale environment, as given by C_{sub} (blue) and C_{tot} (red) respectively, for C1 (left) and C23 (right), over the 36-year period of 1980-2015. See text for a description of these convolutions. The tables below show the lag-zero Spearman correlation of C_{sub} and C_{tot} with seasonal $p(RI)$ and $n(RI)$ statistics in each cluster. Statistical significance is computed with the Student's t-test using 36-2=34 degrees of freedom, as provided by the SciPy statistical package

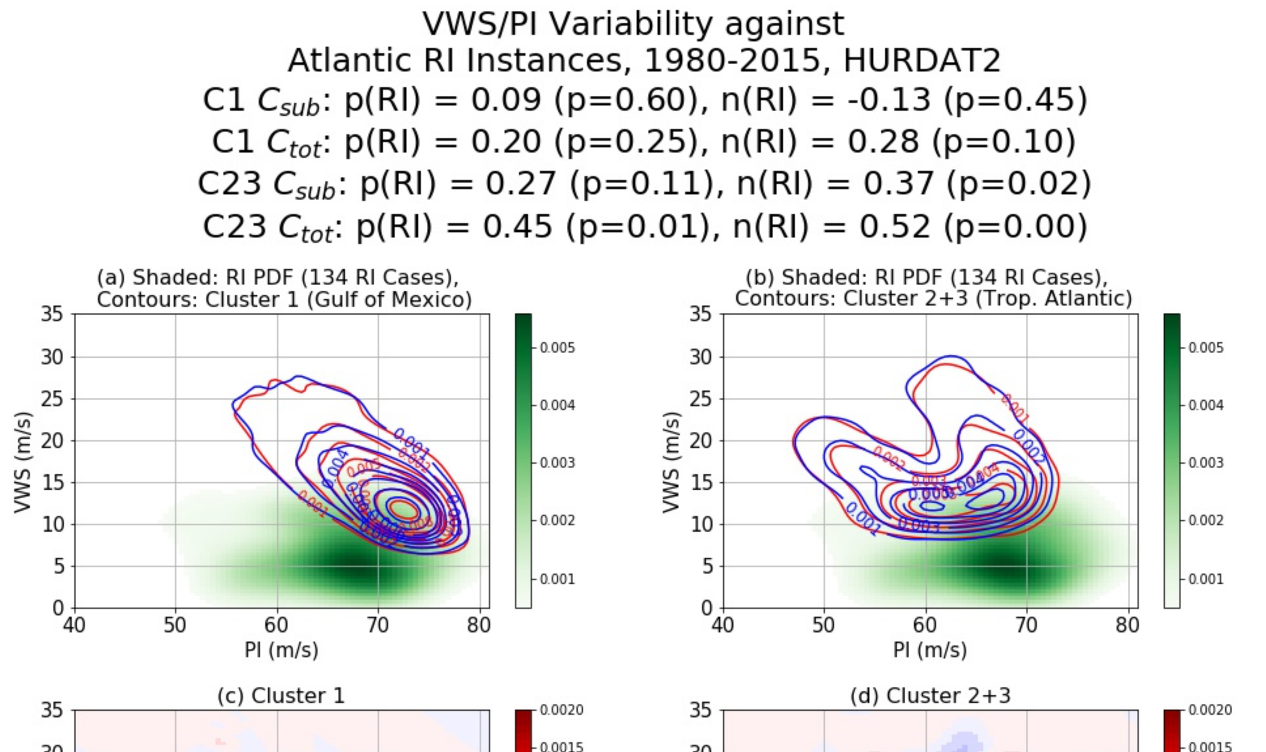

	$p(RI)$		$n(RI)$	
	corr	p	corr	p
C_{sub}	0.09	0.60	-0.13	0.45
C_{tot}	0.20	0.25	0.28	0.10

	$p(RI)$		$n(RI)$	
	corr	p	corr	p
C_{sub}	0.27	0.11	0.37	0.02
C_{tot}	0.45	0.01	0.52	0.00

Fig. 10 As in Figures 8 and 9, but with PDF_{sub} and PDF_{tot} calculated using VWS and PI values weighted by RI density for each cluster, instead of box averages over the cluster region

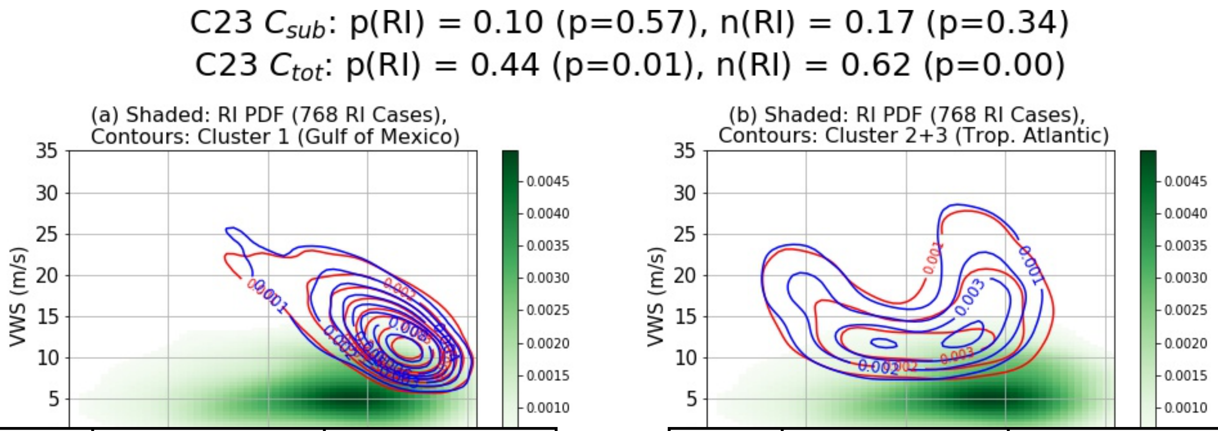

	$p(RI)$		$n(RI)$	
	corr	p	corr	p
C_{sub}	0.21	0.23	0.06	0.72
C_{tot}	0.14	0.43	0.20	0.25

	$p(RI)$		$n(RI)$	
	corr	p	corr	p
C_{sub}	0.10	0.57	0.17	0.34
C_{tot}	0.44	0.01	0.62	0.00

Fig. 11 As in Figure 9, but with PDF_{RI} calculated using all RI events in the North Atlantic, Northwest Pacific and Northeast Pacific combined (shown in Figure 7d)

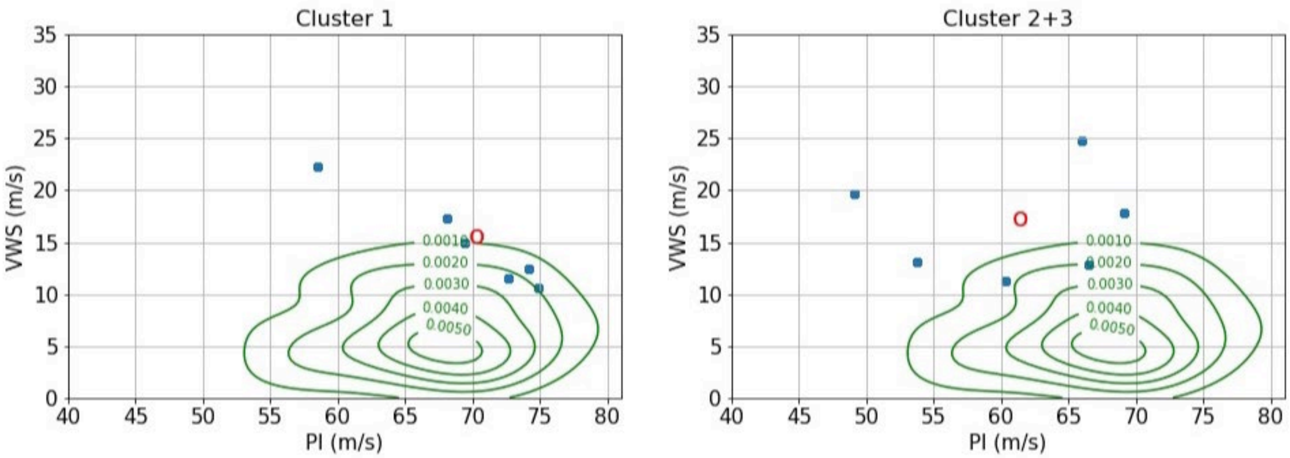

Fig. 12 Two-dimensional probability density function PDF_{RI} (green contours, as in Figure 7a) in the VWS-PI space, superimposed by that of the 1980-2015 MERRA climatological JJASON seasonal cycle $\bar{X}$ (blue) and scalar-mean JJASON climatology $\bar{\bar{X}}$ (red), where $X = VWS, PI$, averaged for C1 (left) and C23 (right)

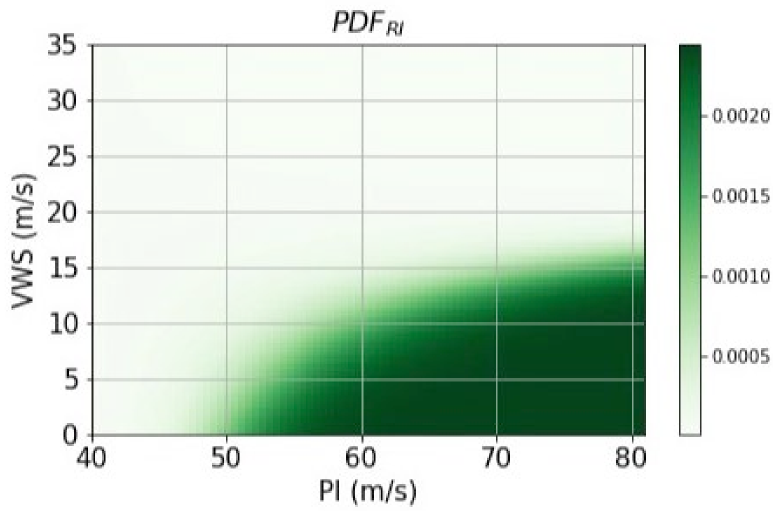

Fig. 13 Best fit of the North Atlantic PDF_{RI} (shown in Figure 7a) to the hyberbolic tangent function in the VWS-PI space, as described in Section 2d

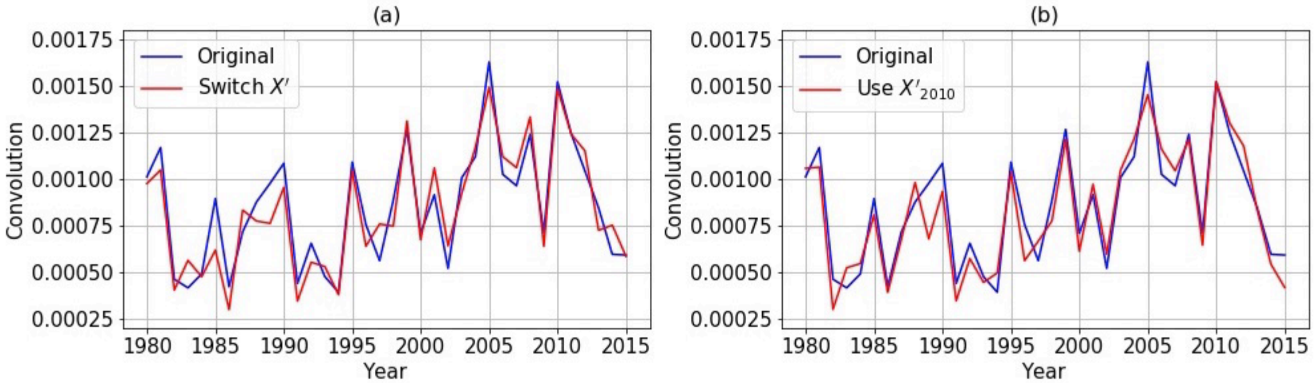

Fig. 14 Impact of subseasonal environmental variability (X') on seasonal RI statistics in C23. (a) Convolution between PDF_{RI} and the two-dimensional PDF computed from $\bar{X}_E + \langle X \rangle_E + X'_E$ (blue) or $\bar{X}_E + \langle X \rangle_E + X'_W$ (red), where X'_E and X'_W represents subseasonal variations in C23 and C1 respectively. See text for a full explanation of these variables. (b) As in (a), but the red plot indicates the convolution computed using subseasonal variations in C23 in 2010 for all years ($\bar{X}_E + \langle X \rangle_E + X'_{2010,E}$)